

## Isotropic Chiral Acoustic Phonons in 3D Quasicrystalline Metamaterials

Yi Chen,<sup>1,\*</sup> Muamer Kadic<sup>1b</sup>,<sup>2</sup> Sébastien Guenneau<sup>1b</sup>,<sup>3</sup> and Martin Wegener<sup>1b</sup>,<sup>4</sup>

<sup>1</sup>*Institute of Applied Physics, Karlsruhe Institute of Technology (KIT), 76128 Karlsruhe, Germany*

<sup>2</sup>*Institut FEMTO-ST, UMR 6174, CNRS, Université de Bourgogne Franche-Comté, 25000 Besançon, France*

<sup>3</sup>*UMI 2004 Abraham de Moivre-CNRS, Imperial College London, London SW7 2AZ, United Kingdom*

<sup>4</sup>*Institute of Nanotechnology, Karlsruhe Institute of Technology (KIT), 76021 Karlsruhe, Germany*



(Received 24 February 2020; accepted 22 May 2020; published 9 June 2020)

The elastic properties of three-dimensional (3D) crystalline mechanical metamaterials, unlike those of amorphous structures, are generally strongly anisotropic—even in the long-wavelength limit and for highly symmetric crystals. Aiming at isotropic linear elastic wave propagation, we therefore study 3D periodic approximants of 3D icosahedral quasicrystalline mechanical metamaterials consisting of uniaxial chiral metarods. Considering the increasing order of the approximants, we approach nearly isotropic effective speeds of sound and isotropic acoustical activity. The latter is directly connected to circularly polarized 3D metamaterial chiral acoustic phonons—for all propagation directions in three dimensions.

DOI: [10.1103/PhysRevLett.124.235502](https://doi.org/10.1103/PhysRevLett.124.235502)

In aiming at effective-medium properties that go beyond those of their ingredient materials, disordered and crystalline rationally designed composites called metamaterials have been investigated extensively throughout recent years [1], including optical [2–6], transport [1], and mechanical properties [7–14]. Often, three-dimensional isotropic effective material properties are desirable in applications. For instance, cubic crystal symmetry guarantees isotropic behavior for electric conduction, particle diffusion, thermal conduction, thermal expansion, and the long-wavelength limit of optics [15]. This statement is not valid though for transverse elastic waves in mechanics, for which cubic and other crystal symmetries generally lead to very highly anisotropic effective properties, even in the strict long-wavelength limit [15–19].

Concerning isotropic elastic properties, this situation leaves one with the possibilities of disordered, extraordinary crystalline, and quasicrystalline architectures. So far, certain isotropic elastic properties have been realized in achiral disordered foams [20], which are effectively isotropic on average, and in achiral extraordinary crystals designed by topology optimization [21]. Following the discovery of atomic 3D quasicrystals [22–28], isotropic achiral elastic properties have also been obtained in 3D quasicrystals [23,29]. However, isotropic elastic properties related to chirality have not been demonstrated in any system by any means so far.

Chiral mechanical metamaterials have emerged recently, but their properties have been highly anisotropic [18,30,31]. Acoustical activity [32–34]—the mechanical counterpart of the well-known phenomenon of optical activity [35]—is a paradigm. Here, chiral phonons instead of the textbook linearly polarized transverse acoustic (TA) phonons are the eigenstates. An incident linear phonon polarization hence

rotates during phonon propagation. Therefore, an application of acoustical activity is polarization mode conversion from one transverse linear polarization to another transverse one, e.g., to the orthogonal transverse one. However, in cubic metamaterial crystals, acoustical activity has been restricted to special propagation directions deviating from the principal cubic axes by no more than just a few degrees [19,36], and yet smaller solid angles around the cubic space diagonals. The underlying reason is fundamental: Acoustical activity is directly connected to circular eigenpolarizations of the two lowest-frequency acoustic-phonon branches, that is, to chiral phonons. To obtain circular polarization, the axis of the phonon wave vector must at least exhibit threefold rotational symmetry [37]—locally, or at least on average. Furthermore, as the effects of chirality generally tend to zero in the strict limit of large samples (bulk) and long wavelengths [19,36], one must depart from the strict long-wavelength limit to obtain appreciable effects of acoustical activity in the bulk.

In this Letter, we investigate the possibility of obtaining isotropic effective elastic behavior related to chirality by introducing 3D quasicrystalline mechanical metamaterials.

Our rational design strategy starts with the cut-and-project method [25,27,38] applied to a 6D simple-cubic lattice of points with lattice constant  $a_{6D}$ . The projection matrix

$$\mathbf{M} = \frac{1}{\sqrt{1 + \tau_0^2}} \begin{pmatrix} \tau_1 & \tau_1 & 0 & -1 & 0 & 1 \\ 0 & 0 & 1 & \tau_1 & 1 & \tau_1 \\ 1 & -1 & -\tau_1 & 0 & \tau_1 & 0 \\ \tau_2 & -\tau_2 & 1 & 0 & -1 & 0 \\ -1 & -1 & 0 & -\tau_2 & 0 & \tau_2 \\ 0 & 0 & \tau_2 & -1 & \tau_2 & -1 \end{pmatrix} \quad (1)$$

acts onto a six-dimensional coordinate vector. The resulting first three components represent the lattice points in 3D physical space, while the other three components represent a fictitious vector in internal space. According to the cut-and-project method for quasicrystals [27] and periodic approximants [25] (see Supplemental Material, Fig. S1 [39]), not all of the resulting points in 3D physical space are accepted as lattice points of the 3D quasicrystal lattice. Rather, only the points for which the internal vectors lie in a certain acceptance domain are used (cf. upper row of Fig. S2 [39]). The projection of the Wigner-Seitz cell of the 6D simple-cubic lattice onto the internal space defines this acceptance domain. We also include those lattice points that lie exactly on the surface of the acceptance domain, which, following [25], lie inside of the acceptance domain if the acceptance domain is shifted by an infinitesimal amount along the body diagonal direction. If the nonzero entries of the matrix in Eq. (1) are chosen to be  $\tau_1 = \tau_2 = \tau_0$ , with the golden ratio  $\tau_0 = (1 + \sqrt{5})/2$ , we obtain a 3D icosahedral quasicrystal. If, instead, we set  $\tau_1 = \tau_0$  and  $\tau_2$  to be a rational approximation of the golden ratio,  $\tau_2 = q/p = F_{n+1}/F_n$  with the elements of the Fibonacci series  $F_n = 1, 1, 2, 3, 5, 8, \dots$  we obtain a 3D crystal. Its three simple-cubic lattice vectors are  $(a_{q/p}, 0, 0)$ ,  $(0, a_{q/p}, 0)$ , and  $(0, 0, a_{q/p})$ , with the lattice constant  $a_{q/p} = 2a_{6D}(q\tau_0 + p)/\sqrt{1 + \tau_0^2}$ . For fractions  $q/p$  approaching  $\tau_0$ , the 3D periodic cell becomes increasingly large and the corresponding 3D crystal approaches a 3D icosahedral quasicrystal. Considering the crystalline approximants is important here because it allows to apply Floquet-Bloch's theorem for the calculation of the phonon band structures. Alternatively, one can possibly solve the eigenvalue problem of an exact quasicrystal lattice by applying Floquet-Bloch's theorem in a higher dimension, and then obtain the band structure through a similar cut-and-project method [26]. Below, we will use  $q/p = 1/1, 2/1, 3/2$ , and  $5/3$ . The corresponding architectures are illustrated in Fig. S2 [39].

To arrive at a practical physical structure, we connect the fictitious points derived from the previous paragraph by ordinary elastic (that is, achiral) homogeneous cylindrical rods in such a way that we obtain nearly isotropic phonon dispersion relations and a negligibly small relative frequency splitting between the lowest two bands in the extended zone scheme for all phonon wave vectors. This aspect is crucial because the frequency splitting between left- and right-handed circularly polarized transverse modes induced by chirality competes with any unwanted effective anisotropy for the achiral case that also lifts the degeneracy between the two orthogonally polarized TA branches. We apply two rules. First, two lattice points are connected if the corresponding 6D lattice points have been nearest neighbors. The resulting architecture can be seen as being composed of two types of rhombohedra, a thinner and a thicker one [see enlargement in Fig. 1(a)]. This 3D

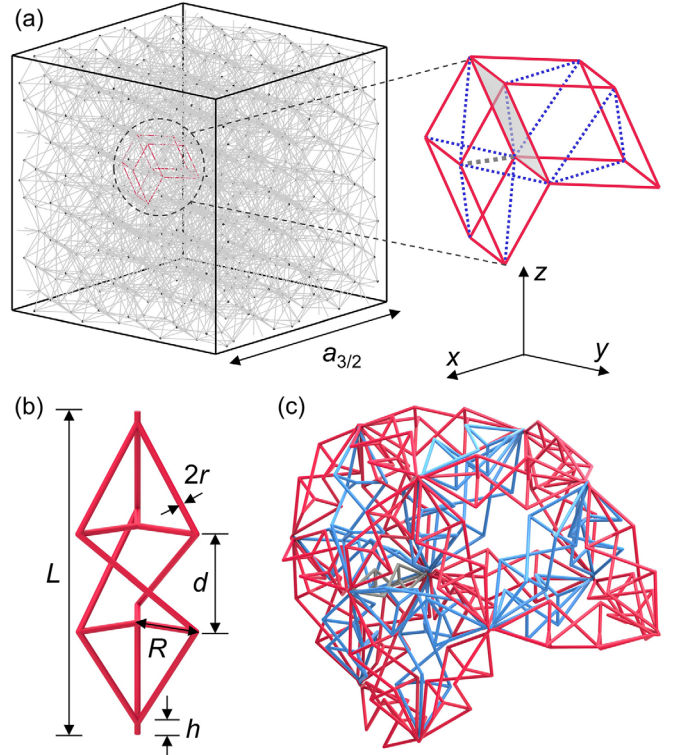


FIG. 1. (a) Illustration of the  $q/p = 3/2$  approximant of a 3D icosahedral quasicrystalline metamaterial. The black points result from the cut-and-project method. The enlarged area highlights three types of segments between these points, i.e., the edges (red), the face diagonals (blue dotted) of the two types of rhombohedra, and the shortest body diagonals (gray dashed) of the thinner rhombohedra. An animated version of the  $3/2$  approximant is shown in Supplemental Material, Video 1 [39]. If we replace each segment by either an achiral homogeneous cylindrical rod or by a homogeneous uniaxial chiral rod, we approach an achiral or a chiral 3D quasicrystal in the limit of large approximant order, respectively. (b) Next, we approximate a homogeneous uniaxial chiral rod with full rotational symmetry by the depicted chiral metarod with threefold rotational symmetry. The metarod is composed of ordinary achiral elastic rods. This approximation is justified for wavelengths large compared to the length  $L$ . (c) Resulting chiral architecture corresponding to the enlarged region in (a). Throughout this Letter, we consider the following normalized parameters:  $d/L = 0.3$ ,  $R/L = 0.2$ ,  $h/L = 0.035$ ,  $r/a_{6D} = 0.01$  (leading to the same rod radius for all rods in the architecture for fixed  $a_{6D}$ ), and fixed  $a_{6D} = 100 \mu\text{m}$ , which is amenable to state-of-the-art 3D laser printing of polymers [18]. Therefore, we use typical polymer parameters for all rods: Young's modulus  $E = 4.18 \text{ GPa}$ , Poisson's ratio  $\nu = 0.4$ , and mass density  $\rho = 1.15 \times 10^3 \text{ kg/m}^3$ .

arrangement of touching rhombohedra is analogous to the 2D aperiodic Penrose tilings [40]. All edges of the rhombohedra have the same length [red in the inset of the Fig. 1(a)]. Second, we additionally introduce segments along the face diagonals (blue dotted) of both types of rhombohedra and along the shortest body diagonal [dashed gray; only one such segment occurs in the inset of Fig. 1(a)]

for the thinner rhombohedra. By increasing the local coordination number, the face-diagonal segments play an important role in decreasing the anisotropy-induced splitting between the two transverse bands along the principal cubic directions. Likewise, the mentioned body diagonals are critical to decrease the anisotropy-induced splitting for wave vectors along the face diagonals of the 3D simple-cubic translational lattice. Without these two additional types of segments, the properties of the metamaterial converge more slowly toward the isotropic case with increasing approximant order. The mentioned three types of links are highlighted by the red, dashed blue, and dashed gray segments in Fig. 1(a). Their respective lengths are  $a_{6D}$ ,  $a_{6D}2/\sqrt{1+\tau_0^2}$ , and  $a_{6D}\sqrt{6-3\tau_0}/\sqrt{1+\tau_0^2}$ . Finally, each segment is replaced by a cylindrical rod composed of an ordinary achiral elastic material. Calculated band structures and contours for these achiral approximants of 3D quasicrystals with rod radius  $r/a_{6D} = 0.01$  are depicted in Figs. S3 and S4, respectively, in the Supplemental Material [39]. The discussed procedure leads to isotropic achiral properties for increasing approximant order.

To achieve chiral metamaterial architectures supporting isotropic chiral phonons, we can conceptually replace each segment of the previous section [i.e., the red, dotted blue, and dashed gray segments in Fig. 1(a)] by a homogeneous uniaxial chiral rod to again obtain an approximant of a true 3D quasicrystal. Unfortunately, rods made of a homogeneous ordinary material with chiral properties do not exist in reality. Therefore, we approximate and replace each rod by the chiral metarod shown in Fig. 1(b). This metarod is composed of ordinary homogeneous achiral elastic rods. Its length  $L$  is scaled according to the segment length. In the limit of vanishing  $R$ , the metarod becomes achiral. In the limit of large  $R$ , neighboring metarods overlap. Our choice is a trade-off. By virtue of the threefold rotational symmetry of the metarod, and independent on its randomly chosen azimuthal angle (see [39]), its effective properties in the limit that the wavelength is large compared to  $L$  are those of a homogeneous uniaxial chiral rod, supporting chiral phonons propagating along the rod axis. Purely geometrically speaking, the truss lattice itself [cf. Fig. 1(c)] does not converge to a 3D quasicrystal.

For the  $q/p = 1/1$ ,  $2/1$ ,  $3/2$ , and  $5/3$  approximants considered below, this procedure leads to 32, 136, 576, and 2240 points within one periodic cell, respectively, and to 228, 920, 3398, and 16 768 chiral metarods within one periodic cell, respectively. To deal with periodic cells containing so many rods, we treat all rods by using Timoshenko-beam theory and COMSOL Multiphysics® (MUMPS solver) [41]. This approximation is justified because the rods are very slender [ $r/a_{6D} = 0.01$  in Fig. 1(b)]. For the metarod shown in Fig. 1(b), a direct comparison to continuum mechanics is provided in Fig. S5 [39].

In Figs. 2(a)–2(d), we plot the calculated phonon dispersion relations along cubic face diagonals and principal

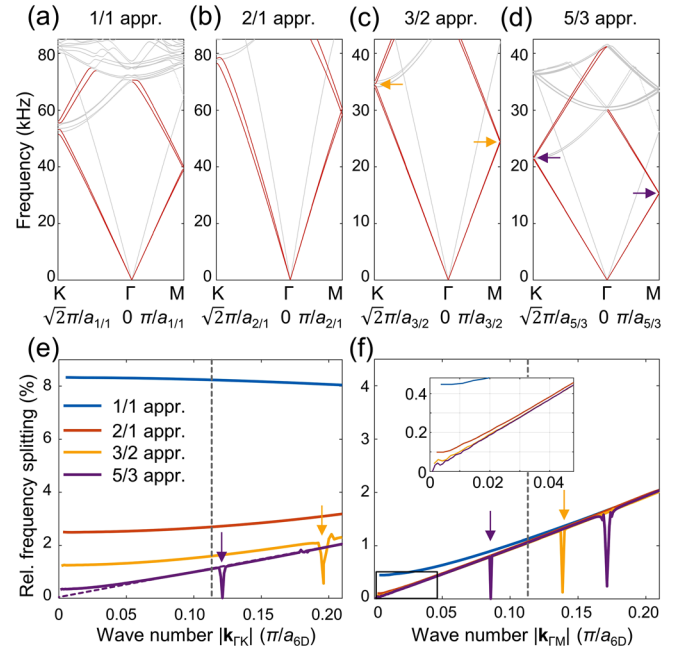


FIG. 2. Calculated phonon dispersion relations for approximant architectures as illustrated in Fig. 1 for propagation along a cubic face diagonal ( $\Gamma\mathbf{K}$  direction, left) and a principal cubic direction ( $\Gamma\mathbf{M}$  direction, right). (a)  $q/p = 1/1$ , (b)  $q/p = 2/1$ , (c)  $q/p = 3/2$ , and (d)  $q/p = 5/3$ . The lowest two transverse bands and their backfolded parts are colored in red, the other less important bands are plotted in gray. These data are shown in magnified form in Fig. S6 [39]. (e) and (f) exhibit the relative frequency splitting,  $2(f_2 - f_1)/(f_2 + f_1)$ , between the two transverse bands. The colors for the four approximants are indicated in the legend. (e)  $\Gamma\mathbf{K}$  direction. (f)  $\Gamma\mathbf{M}$  direction. The results shown in Figs. 3 and 4 have been evaluated for the wave number indicated by the dashed gray straight lines.

cubic directions for the  $q/p = 1/1$ ,  $2/1$ ,  $3/2$ , and  $5/3$  approximants. The lowest two transverse phonon branches and their backfolded parts are colored in red. The other, less important, bands are colored in gray. A frequency splitting between the two red transverse bands is clearly visible for both propagation directions. This splitting can generally have two different origins: Unwanted anisotropy and wanted chirality. The anisotropy results in linearly or elliptically polarized eigenmodes, whereas chirality alone ideally leads to chiral phonons connected to circularly polarized eigenmodes. In the long-wavelength limit of a periodic structure, the anisotropy-induced relative frequency splitting is independent of the wave number  $|\mathbf{k}|$ . In contrast, the chirality-induced splitting should vanish  $\propto |\mathbf{k}|$  in the long-wavelength limit, for which classical Cauchy elasticity applies [15]. Therefore, we expect the splitting at  $|\mathbf{k}| = 0$  to be anisotropy-induced only, which is unwanted. It is thus instructive to plot the relative frequency splitting,  $2(f_2 - f_1)/(f_2 + f_1)$ , versus the phonon wave number  $|\mathbf{k}|$  in Figs. 2(e) and 2(f). The dips in the curves indicated by the arrows occur on the edge of the first Brillouin zone for the corresponding approximant periodic cell. Clearly, the

relative frequency splitting at  $|\mathbf{k}| = 0$  converges to zero with increasing approximant order [see Figs. 2(e) and 2(f)]. For the highest approximant order numerically accessible to us, i.e.,  $q/p = 5/3$ , the relative splitting for  $|\mathbf{k}| = 0$  is about 0.3% for wave vectors along the cubic face diagonals [see Fig. 2(e)] and less than 0.03% for the principal cubic directions [see Fig. 2(f)]. As expected from micropolar continuum elasticity [19], the chirality-induced relative splitting converges toward a behavior  $\propto |\mathbf{k}|$  [see the purple dashed straight line in Fig. 2(e)]. At the indicated gray line at  $|\mathbf{k}| = 1/9(\pi/a_{6D})$ , chirality-induced splitting dominates over the anisotropy-induced splitting and we expect chiral phonon polarizations for the two sets of directions considered. Indeed, inspection of the corresponding eigenmodes reveals circular phonon polarization [see Supplemental Material, Fig. S7 and Videos 2 and 3 [39]].

Yet more importantly, based on our entire design process, we expect an isotropic chiral behavior of the acoustic phonons in the limit of increasing approximant order. To numerically test this conjecture, we visualize the three-dimensional direction dependence of the eigenfrequencies  $f_1$  and  $f_2$  in Fig. 3 and of the eigenmode

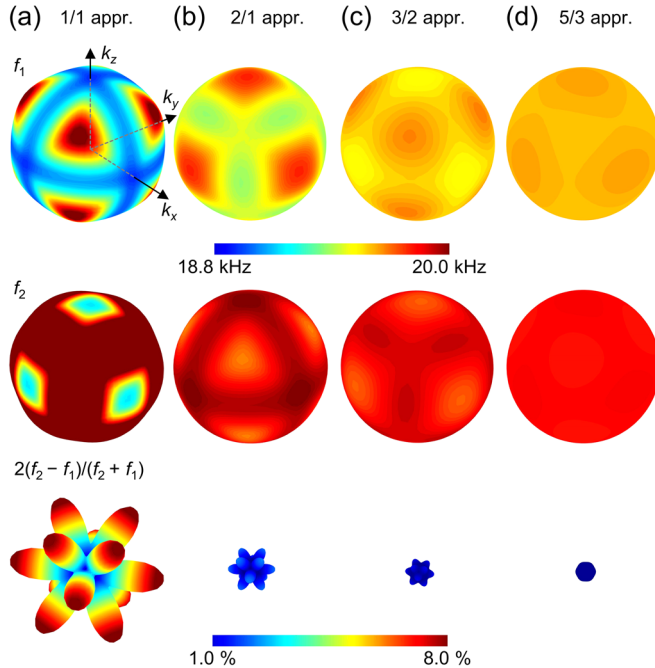


FIG. 3. Calculated results for increasing order (from left to right) of 3D quasicrystal approximants for  $|\mathbf{k}| = 1/9(\pi/a_{6D})$  [cf. dashed gray lines in Figs. 2(e) and 2(f)]. (a)  $q/p = 1/1$ , (b)  $q/p = 2/1$ , (c)  $q/p = 3/2$ , and (d)  $q/p = 5/3$ . In the first two rows, we depict the direction dependence of the two transverse phonon eigenfrequencies,  $f_1$  and  $f_2$  on a false-color scale. In addition, the length of the vector from the origin to the surface of the plot is proportional to the eigenfrequency for this propagation direction. In the third row, we depict the relative frequency splitting between the two transverse eigenfrequencies,  $2(f_2 - f_1)/(f_2 + f_1)$ , in the same manner.

polarizations in Fig. 4 [again for a fixed modulus of the phonon wave vector of  $|\mathbf{k}| = 1/9(\pi/a_{6D})$ ]. For the  $q/p = 5/3$  approximant in Fig. 3, the frequency  $f_1$  varies only between a minimum of 19.61 kHz and a maximum of 19.66 kHz.  $f_2$  varies between 19.82 kHz and 19.86 kHz. The corresponding relative frequency splitting  $2(f_2 - f_1)/(f_2 + f_1) \approx 1\%$  is nearly isotropic, too. In the ideal isotropic limit,  $f_1$ ,  $f_2$ , and  $2(f_2 - f_1)/(f_2 + f_1)$  should be constant. In Fig. 4, we visualize the eigenpolarizations of the two transverse phonon bands. This is accomplished in two different ways. First, we define the polarization degree as the ratio  $\zeta$  of the minor and major axes of the polarization ellipse formed by the mean displacement vector of the periodic cell versus time:  $\zeta = 1$  corresponds to circular polarization,  $\zeta = 0$  to linear polarization, and values in between to elliptical polarization. In the top row of Fig. 4, we false-color code  $\zeta$  onto the surface of a sphere in 3D wave vector space. From this representation, one can see that the ideal of constant  $\zeta = 1$  is approached with increasing approximant order. However, one cannot see the orientation of the polarization ellipse. Therefore, we depict in the bottom row of Fig. 4 the real-space trace of the mean displacement vector, again for the two transverse bands,  $i = 1, 2$ . Obviously, very nearly circular polarization is achieved for all wave vector directions for the

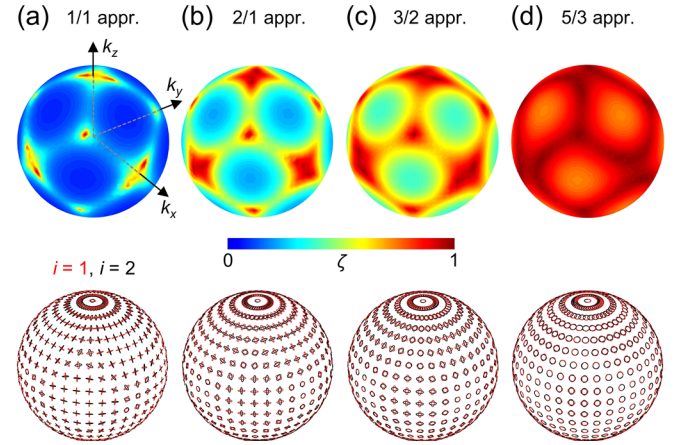


FIG. 4. Calculated results for increasing order (from left to right) of 3D quasicrystal approximants for  $|\mathbf{k}| = 1/9(\pi/a_{6D})$  [cf. dashed gray lines in Figs. 2(e) and 2(f)]. (a)  $q/p = 1/1$ , (b)  $q/p = 2/1$ , (c)  $q/p = 3/2$ , and (d)  $q/p = 5/3$ . The first row exhibits the polarization degree,  $\zeta$ , on a false-color scale (cf. Fig. 3).  $\zeta = 0$  corresponds to linear polarization and  $\zeta = 1$  to circular polarization. The second row shows real-space trajectories of the phonon displacement vector versus time (mean over one periodic cell), i.e., a circle corresponds to circular phonon polarization, an ellipse to elliptical polarization, and a line to linear polarization. The center of each miniature on the sphere indicates the corresponding wave vector direction in 3D. The behavior of the two transverse phonon bands, with indices  $i = 1$  and  $i = 2$ , is shown in red and black, respectively. For the 5/3 approximant, chiral phonons are obtained for all phonon propagation directions in 3D.

highest  $q/p = 5/3$  approximant, whereas linear or elliptical polarizations still dominate for the 1/1 and the 2/1 approximants. If the local coordination number is reduced by considering only the red connections in Fig. 1(a), the isotropic ideal is not yet reached for the 5/3 approximant [cf. Fig. S8 [39]].

In conclusion, we have presented a rational design of truss-based chiral 3D mechanical metamaterials exhibiting nearly isotropic chiral acoustic phonons (and as a special limit also isotropic achiral acoustic phonons). Our design approach is based on 3D quasicrystal approximants of increasing order. Intuitively, for sufficiently large wavelengths and on average over the course of propagation through the infinite 3D periodic approximant, the elastic wave feels an isotropic chiral medium with complete rotational symmetry around any wave propagation direction. This averaging should make the architecture robust against disorder but comes at the price of reduced chiral effects. Here, we achieve an isotropic relative frequency splitting of 1%, which compares to maxima over 10% in highly anisotropic cubic 3D metamaterial crystals [31]. Future experimental realizations of our proposal appear possible based on advanced 3D additive manufacturing. However, the more than ten thousand chiral metarods per 3D approximant periodic cell pose a formidable challenge.

Y.C. acknowledges support by the Alexander von Humboldt Foundation and by the National Natural Science Foundation of China (Contract No. 11802017). This research has additionally been funded by the Deutsche Forschungsgemeinschaft (DFG, German Research Foundation) under Germany's Excellence Strategy via the Excellence Cluster 3D Matter Made to Order (EXC-2082/1-390761711), which has also been supported by the Carl Zeiss Foundation through the Carl-Zeiss-Foundation-Focus@HEiKA, by the State of Baden-Württemberg, and by the Karlsruhe Institute of Technology (KIT). We further acknowledge support by the Helmholtz program Science and Technology of Nanosystems (STN), and by the associated KIT project Virtual Materials Design (VIRTMAT). M. K. is grateful for support by the EIPHI Graduate School (Contract No. ANR-17-EURE-0002) and by the French Investissements d'Avenir program, project ISITEBFC (Contract No. ANR-15-IDEX-03).

\* yi.chen@partner.kit.edu; chenyi221@gmail.com

- [1] M. Kadic, G. W. Milton, M. van Hecke, and M. Wegener, *Nat. Rev. Phys.* **1**, 198 (2019).
- [2] A. DellaVilla, S. Enoch, G. Tayeb, V. Pierro, V. Galdi, and F. Capolino, *Phys. Rev. Lett.* **94**, 183903 (2005).
- [3] E. Plum, X. X. Liu, V. A. Fedotov, Y. Chen, D. P. Tsai, and N. I. Zheludev, *Phys. Rev. Lett.* **102**, 113902 (2009).
- [4] A. Alu and N. Engheta, *Phys. Rev. Lett.* **103**, 143902 (2009).
- [5] W. Cai and V. M. Shalae, *Optical Metamaterials* (Springer, New York, 2010), Vol. 10.
- [6] I. Fernandez-Corbaton, C. Rockstuhl, P. Ziemke, P. Gumbsch, A. Albiez, R. Schwaiger, T. Frenzel, M. Kadic, and M. Wegener, *Adv. Mater.* **31**, 1807742 (2019).
- [7] G. Milton and R. Willis, *Proc. R. Soc. A* **463**, 855 (2007).
- [8] X. Liu, G. Hu, G. Huang, and C. Sun, *Appl. Phys. Lett.* **98**, 251907 (2011).
- [9] R. Zhu, X. Liu, G. Hu, C. Sun, and G. Huang, *Nat. Commun.* **5**, 5510 (2014).
- [10] S. H. Kang, S. Shan, A. Košmrlj, W. L. Noorduin, S. Shian, J. C. Weaver, D. R. Clarke, and K. Bertoldi, *Phys. Rev. Lett.* **112**, 098701 (2014).
- [11] S. Krödel, N. Thomé, and C. Daraio, *Extreme Mech. Lett.* **4**, 111 (2015).
- [12] Y. Achaoui, B. Ungureanu, S. Enoch, S. Brûlé, and S. Guenneau, *Extreme Mech. Lett.* **8**, 30 (2016).
- [13] C. Coulais, C. Kettenis, and M. van Hecke, *Nat. Phys.* **14**, 40 (2018).
- [14] W. Wang, Y. Jin, W. Wang, B. Bonello, B. Djafari-Rouhani, and R. Fleury, *Phys. Rev. B* **101**, 024101 (2020).
- [15] A. Authier, *Physical Properties of Crystals, International Tables for Crystallography* (Springer, New York, 2003), Vol. D.
- [16] C. Lin, T. Fang, T. Zhang, S. Niu, G. Cheng, and Z. Shi, *Solid State Commun.* **54**, 803.
- [17] S. Babaee, J. Shim, J. C. Weaver, E. R. Chen, N. Patel, and K. Bertoldi, *Adv. Mater.* **25**, 5044 (2013).
- [18] T. Frenzel, M. Kadic, and M. Wegener, *Science* **358**, 1072 (2017).
- [19] Y. Chen, T. Frenzel, S. Guenneau, M. Kadic, and M. Wegener, *J. Mech. Phys. Solids* **137**, 103877 (2020).
- [20] R. Lakes, *Science* **235**, 1038 (1987).
- [21] A. Radman, X. Huang, and Y. Xie, *Eng. Optim.* **45**, 1331 (2013).
- [22] D. Shechtman, I. Blech, D. Gratias, and J. W. Cahn, *Phys. Rev. Lett.* **53**, 1951 (1984).
- [23] P. Bak, *Phys. Rev. B* **32**, 5764 (1985).
- [24] J. E. S. Socolar, T. C. Lubensky, and P. J. Steinhardt, *Phys. Rev. B* **34**, 3345 (1986).
- [25] J. Los, T. Janssen, and F. Gähler, *J. Phys. I (France)* **3**, 107 (1993).
- [26] A. W. Rodriguez, A. P. McCauley, Y. Avniel, and S. G. Johnson, *Phys. Rev. B* **77**, 104201 (2008).
- [27] C. Janot, *Quasicrystals: A Primer*, Monographs on the Physics and Chemistry of Materials (Oxford University Press, Oxford, 2012).
- [28] T. Janssen, G. Chapuis, and M. De Boissieu, *Aperiodic Crystals: From Modulated Phases to Quasicrystals* (Oxford University Press, Oxford, 2018), Vol. 20.
- [29] P. S. Spoor, J. D. Maynard, and A. R. Kortan, *Phys. Rev. Lett.* **75**, 3462 (1995).
- [30] Z. Rueger and R. S. Lakes, *Phys. Rev. Lett.* **120**, 065501 (2018).
- [31] J. Reinbold, T. Frenzel, A. Münchinger, and M. Wegener, *Materials* **12**, 3527 (2019).
- [32] L. Whyte, *Nature (London)* **182**, 198 (1958).
- [33] D. L. Portigal and E. Burstein, *Phys. Rev.* **170**, 673 (1968).

- [34] K. V. Bhagwat and R. Subramanian, *Acta Crystallogr. Sect. A* **44**, 551 (1988).
- [35] I. V. Lindell, A. H. Sihvola, S. A. Tretyakov, and A. J. Viitanen, *Electromagnetic Waves in Chiral and Bi-Isotropic Media* (Artech House Boston, London, 1994).
- [36] T. Frenzel, J. Köpfler, E. Jung, M. Kadic, and M. Wegener, *Nat. Commun.* **10**, 3384 (2019).
- [37] I. Fernandez-Corbaton, *Opt. Express* **21**, 29885 (2013).
- [38] M. Duneau and A. Katz, *Phys. Rev. Lett.* **54**, 2688 (1985).
- [39] See Supplemental Material at <http://link.aps.org/supplemental/10.1103/PhysRevLett.124.235502> for illustration of the generalized cut-and-project method, details on the 3D chiral approximants, details of numerical procedure, justification of the Timoshenko-beam model, results of isotropic achiral lattices, examples of circularly polarized eigenmodes, and influence of coordination number.
- [40] R. Penrose, *Bull. Inst. Math. Appl.* **10**, 266 (1974).
- [41] T. J. Hughes, *The Finite Element Method* (Dover Publications, New York, 2000).